Pergamon

0020–7683(95)00259–6

DESIGN OF SIMPLE LOW ORDER FINITE ELEMENTS FOR LARGE STRAIN ANALYSIS OF NEARLY INCOMPRESSIBLE SOLIDS

E. A. de SOUZA NETO, D. PERIĆ, M. DUTKO and D. R. J. OWEN

Department of Civil Engineering, University of Wales Swansea, Singleton Park,
Swansea SA2 8PP, U.K.

Abstract—A simple four-node quadrilateral and an eight-node hexahedron for large strain analysis of nearly incompressible solids are proposed. Based on the concept of deviatoric/volumetric split and the replacement of the compatible deformation gradient with an assumed modified counterpart, the formulation developed is applicable to arbitrary material models. The closed form of the corresponding exact tangent stiffnesses, which have a particularly simple structure, is derived. It ensures asymptotically quadratic rates of convergence of the Newton-Raphson scheme employed in the solution of the implicit finite element equilibrium equations. From a practical point of view, the incorporation of the proposed elements into existing codes is straightforward. It requires only small changes in the routines of the standard displacement based 4-node quadrilateral and 8-node brick. A comprehensive set of numerical examples, involving hyperelasticity as well as multiplicative elasto-plasticity, is provided. It illustrates the performance of the proposed elements over a wide range of applications, including strain localisation problems, metal forming simulation and adaptive analysis. Copyright © 1996 Elsevier Science Ltd.

1. INTRODUCTION

It is a well known fact that the performance of low order kinematically based finite elements is extremely poor near the incompressible limit. Problems of practical engineering interest for which incompressibility plays a crucial role include the analysis of rubbery solids, typically modelled as incompressible hyperelastic materials, as well as elastoplastic simulations under plastic dominant deformations and the assumption of isochoric plastic flow. In such situations, spurious *locking* frequently occurs as a consequence of the inability of low order interpolation polynomials to adequately represent general volume preserving displacement fields. However, due to their simplicity, low order elements are often preferred in large scale computations and several formulations have been proposed to allow their use near the incompressible limit. Within the context of the geometrically linear theory, the class of assumed enhanced strain methods described by Simo and Rifai (1990), which incorporates popular procedures such as the classical incompatible modes formulation (Taylor *et al.*, 1976) and *B-bar* methods (Hughes, 1980), is well established and is employed with success in a number of existing commercial finite element codes. In the geometrically non-linear regime, however, the enforcement of incompressibility is substantially more demanding and the development of robust and efficient low order finite elements is by no means trivial. To tackle such a problem, different approaches have been proposed in the computational literature. Among others, the class of mixed variational methods developed by Simo *et al.* (1985), the mixed *u/p* formulation proposed by Sussman and Bathe (1987), the non-linear B-bar methodology adopted by Moran *et al.* (1990) and the family of enhanced elements of Simo and Armero (1992) are particularly important. One aspect that should be observed here is that, in addition to handling incompressibility, robust formulations should also be able to cope with the extra requirements that different problems may present. For instance, in applications such as the prediction of failure in metal forming processes, the ability to capture strain localisation phenomena becomes crucial; in problems involving extremely large strains, frequently encountered in the analysis of rubbery materials and metal forming simulations, it is not unusual that a solution can be obtained only if adaptive mesh refinement is employed. Thus, since a single formulation is normally not

sufficiently robust to produce an optimal performance under a very wide range of conditions, the design of low order finite elements for large strain analysis of quasi-incompressible materials remains an open issue.

The purpose of this work is the development of a simple 4-node quadrilateral and a simple 8-node hexahedron for finite strain analysis of nearly incompressible solids. The elements are based on the concept of multiplicative deviatoric/volumetric split in conjunction with the replacement of the compatible deformation gradient field with an assumed modified counterpart. The resulting formulation can be used regardless of the material model adopted. In addition, the strain driven format of the algorithms for integration of inelastic constitutive equations of the purely kinematic formulation is maintained. Despite some conceptual similarities, the present approach cannot be regarded as a geometrically non-linear extension of the *B-bar* methodology. In order to preserve the asymptotically quadratic rates of convergence of the Newton-Raphson scheme in implicit finite element computations, the closed form of the corresponding consistent tangent stiffnesses is derived. It has a particularly simple structure so that existing codes that support the conventional 4-node displacement based quadrilateral (or 8-node hexahedron, if 3-D analysis is sought) can be easily adapted to incorporate the new elements. For convenience, the changes required in the conventional displacement based element routines are summarized in Boxes 1 and 2. This paper is organized as follows. The proposed elements are introduced in Section 2. Their formulation as well as aspects of computational implementation are discussed in detail. Numerical examples are provided in Section 3. They illustrate the performance of the proposed formulation under a wide variety of conditions involving hyperelastic as well as elasto-plastic material models. The problems considered range from strain localization phenomena and metal forming simulation to finite strain adaptive analysis. Finally, in Section 4, some conclusions are presented.

2. THE LOW ORDER ELEMENTS FOR FINITE STRAIN PROBLEMS

Central to the developments presented below is the concept of multiplicative split of the deformation gradient, F, into deviatoric (volume preserving) and volumetric (dilatational) contributions. This multiplicative decomposition has been exploited by Simo (1985), Moran *et al.* (1990) and Simo and Taylor (1991) in the treatment of the incompressibility constraint in finite deformation problems. It consists of splitting the deformation gradient according to the expression:

$$\mathbf{F} = \mathbf{F}_d \mathbf{F}_v, \tag{1}$$

where $\mathbf{F}_d$ and $\mathbf{F}_v$ are, respectively, the deviatoric and volumetric components of F, defined by:

$$\mathbf{F}_d = (\det [\mathbf{F}])^{-1/3} \mathbf{F}, \quad \mathbf{F}_v = (\det [\mathbf{F}])^{1/3} \mathbf{I}. \tag{2}$$

In the expressions above, I denotes the identity tensor and det[·] stands for the determinant of [·]. Note that, by construction, $\mathbf{F}_d$ and $\mathbf{F}_v$ satisfy:

$$\det [\mathbf{F}_d] = 1, \quad \det [\mathbf{F}_v] = \det [\mathbf{F}]. \tag{3}$$

2.1. *Stress computation. The modified deformation gradient*

Consider an ordinary displacement based 4-node quadrilateral and an 8-node hexahedron, with local coordinates denoted ξ, as illustrated in Fig. 1. Typically, the numerical integration of the element internal force vector requires the computation of the stresses at a prescribed number of Gauss points and, for geometrically non-linear problems, the stresses are obtained from the deformation gradient by means of constitutive functionals.
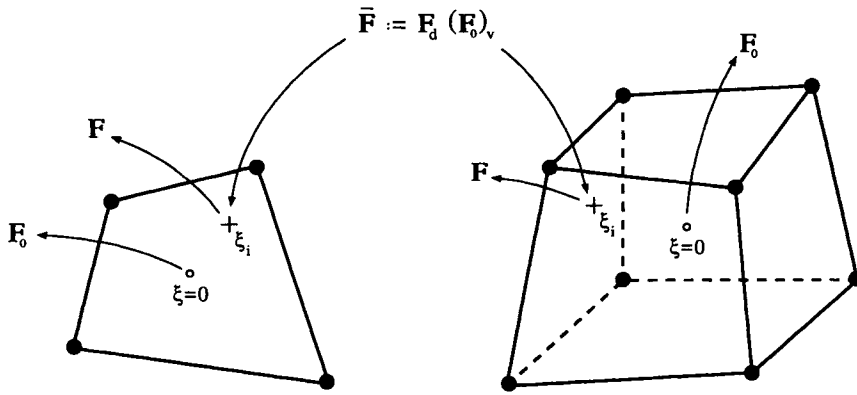
$$\bar{\mathbf{F}} := \mathbf{F}_d\,(\mathbf{F}_0)_v$$

Fig. 1. The proposed 4-node quadrilateral and 8-node hexahedron.

Let $\mathbf{F}$ be the deformation gradient computed from the standard (bi-linear for the quadrilateral and tri-linear for the hexahedron) interpolation of the displacement field at a generic integration point i, with coordinate ξ_i, indicated in Fig. 1. For the conventional elements, the Cauchy stress tensor, σ, in the case of elastic materials is determined at each integration point by

$$\sigma = \hat{\sigma}(\mathbf{F}), \tag{4}$$

where $\hat{\sigma}$ is the corresponding elastic constitutive functional† for the Cauchy stress.

The basic objective here is to design a simple 4-node quadrilateral and a simple 8-node hexahedron that circumvent, in the non-linear range, the spurious locking exhibited by the standard bi-linear and tri-linear elements near the incompressible limit. The key idea underlying the present formulation is the use of an assumed modified deformation gradient to compute the stresses in (4). Firstly, the volumetric/deviatoric split (2) is applied to the deformation gradient $\mathbf{F}$ at the Gauss point of interest as well as to the deformation gradient $\mathbf{F}_0$ that results from the conventional displacement interpolation at the centroid of the element, $\xi = 0$ (see Fig. 1):

$$\mathbf{F} = \mathbf{F}_d\mathbf{F}_v, \quad \mathbf{F}_0 = (\mathbf{F}_0)_d(\mathbf{F}_0)_v.$$

The *modified deformation gradient*, $\bar{\mathbf{F}}$, is then defined as the composition of the deviatoric component of $\mathbf{F}$ with the volumetric component of $\mathbf{F}_0$, i.e.,

$$\bar{\mathbf{F}} := \mathbf{F}_d(\mathbf{F}_0)_v = \left(\frac{\det[\mathbf{F}_0]}{\det[\mathbf{F}]}\right)^{1/3}\mathbf{F}. \tag{5}$$

Having defined the modified deformation gradient, the proposed 4 and 8-node elements are obtained by replacing $\mathbf{F}$ and $\bar{\mathbf{F}}$ in (4). Thus, for the present elements, the Cauchy stress at each Gauss point is computed as

---

† For inelastic materials, incremental constitutive functionals are used instead. In these cases, considering a typical time interval $[t_n, t_{n+1}]$, the stress is evaluated as

$$\sigma_{n+1} = \hat{\sigma}(V_n, \mathbf{F}_{n+1}),$$

where V_n is the set of history dependent internal variables whose values at t_n are known and $\mathbf{F}_{n+1}$ is the deformation gradient at the end of the interval. The functional $\hat{\sigma}$ in this case represents an algorithm for integration of path dependent constitutive equations such as, for instance, the standard return mappings employed in classical elastoplasticity (Ortiz and Popov, 1985; Simo and Hughes, 1987).

$$\sigma = \hat{\sigma}(\bar{\mathbf{F}}). \tag{6}$$

Remark 2.1 By construction of $\bar{\mathbf{F}}$, the deviatoric/volumetric split of the modified deformation gradient gives

$$\begin{cases} \bar{\mathbf{F}}_d = (\det{[\mathbf{F}]})^{-1/3}\mathbf{F} = \mathbf{F}_d \\ \bar{\mathbf{F}}_v = (\det{[\mathbf{F}_0]})^{1/3}\mathbf{I} = (\mathbf{F}_0)_v \end{cases} \tag{7}$$

i.e., the deviatoric component of $\bar{\mathbf{F}}$ coincides with the current (integration point) deviatoric deformation gradient while its volumetric part corresponds to the dilatation at the centroid of the element. In view of (6), this implies that, for materials whose deviatoric and volumetric responses are decoupled, the present formulation results in constant pressure distributions throughout one element.   □

2.1.1. *The internal force vector.* The finite element version of the principle of virtual work (equilibrium) reads:

$$\mathbb{F}^{INT} - \mathbb{F}^{EXT} = 0 \tag{8}$$

where $\mathbb{F}^{EXT}$ is the external load vector evaluated in the standard fashion and, for the present elements, $\mathbb{F}^{INT}$ is obtained from the assemblage of the element internal force vectors expressed, in the spatial configuration, by:

$$\mathbb{F}_e^{INT} = \int_{\varphi(\Omega^e)} \mathbb{B}^T \{\hat{\sigma}(\bar{\mathbf{F}})\}\,\mathrm{d}v \tag{9}$$

Here, $\mathbb{B}$ denotes the standard discrete spatial symmetric gradient operator and $\{\hat{\sigma}(\bar{\mathbf{F}})\}$ is the finite element vector of Cauchy stress components.

Remark 2.2. As far as the computation of the internal force vector is concerned, the *only* difference between the present elements and their conventional displacement based counterparts is the replacement of $\mathbf{F}$ and $\bar{\mathbf{F}}$ in the computation of the Cauchy stress. Thus, in addition to the evaluation of $\mathbf{F}$ and σ at each Gauss point—procedures carried out normally for the standard elements—the proposed elements require only the evaluation of $\det[\mathbf{F}_0]$, at their centroids, and the computation of $\bar{\mathbf{F}}$ which, from its definition (5), is obtained by simply multiplying $\mathbf{F}$ by a *scalar* factor. The added computational effort is, therefore, minimal. We emphasize that, as for the conventional elements, 4 and 8 point Gauss quadratures are adopted here for the present 4-node quadrilateral and 8-node hexahedron respectively.   □

Remark 2.3. Geometrically non-linear extensions of the so-called *B-bar* methods, such as the class of elements proposed by Moran *et al.* (1990) and particular cases of the general methodology developed by Simo *et al.* (1985), are also based on the replacement of the compatible deformation gradient with an assumed modified counterpart defined similarly to (5). However, in contrast to such procedures, modified gradient operators (or *B-bar* matrices) do not take part in the present formulation. Note that the *standard* B-matrix appears in (9). This is due to the fact that, here, the assumed deformation gradient has been introduced in the stress constitutive functional rather than in the corresponding strain energy functional. As we shall see in what follows, the present approach allows for a

straightforward adaptation of existing displacement based element routines to incorporate the new elements.   □

2.2. Consistent linearization. The tangent stiffness matrix

In the context of implicit finite element computations, the linearization of the system (8) is the basis of the Newton-Raphson scheme for solution of the discrete non-linear boundary value problem. Calling $\mathbb{R}$ the out-of-balance force and $\mathbb{U}$ the finite element global displacement vector and assuming that external loads do not depend on the configuration,† we can write the equilibrium statement as

$$\mathbb{R}(\mathbb{U}) := \mathbb{F}^{INT}(\mathbb{U}) - \mathbb{F}^{EXT} = 0, \tag{10}$$

and, during a typical Newton-Raphson iteration k, the following linear system is solved for the increment of displacement $\Delta\mathbb{U}^{(k)}$:

$$\mathbb{K}(\mathbb{U}^{(k)})[\Delta\mathbb{U}^{(k)}] = -\mathbb{R}(\mathbb{U}^{(k)}), \tag{11}$$

where the tangent stiffness $\mathbb{K}$ is defined by the directional derivative formula:

$$\mathbb{K}(\mathbb{U})[\Delta\mathbb{U}] = \frac{d}{d\varepsilon}\bigg|_{\varepsilon=0} \mathbb{R}(\mathbb{U}+\varepsilon\,\Delta\mathbb{U}) = \frac{d}{d\varepsilon}\bigg|_{\varepsilon=0} \mathbb{F}^{INT}(\mathbb{U}+\varepsilon\,\Delta\mathbb{U}). \tag{12}$$

Proposition 2.1. Let the internal force vector $\mathbb{F}^{INT}$ be defined as the assembly of the element vectors (9). Then, the corresponding tangent stiffness, $\mathbb{K}$, is obtained by the assemblage of the element stiffness matrices:

$$\mathbb{K}_e = \underbrace{\int_{\varphi(\Omega_e)} \mathbb{G}^T[\mathbf{a}]_{\mathbf{F}=\bar{\mathbf{F}}}\mathbb{G}\,dv}_{\substack{\text{standard element} \\ \text{stiffness at } \mathbf{F}=\bar{\mathbf{F}}}} + \underbrace{\int_{\varphi(\Omega_e)} \mathbb{G}^T[\mathbf{q}](\mathbb{G}_0-\mathbb{G})\,dv}_{\substack{\text{additional} \\ \text{stiffness}}}, \tag{13}$$

where $\mathbb{G}$ is the *standard* discrete spatial gradient operator, $\mathbb{G}_0$ is the gradient operator at the element centroid, $[\mathbf{a}]_{\mathbf{F}=\bar{\mathbf{F}}}$ denotes the matrix form of the *spatial elasticity tensor*,‡

$$a_{ijkl} = \frac{1}{\det[\mathbf{F}]}F_{jp}F_{tq}A_{ipkq}, \tag{14}$$

evaluated at $\mathbf{F} = \bar{\mathbf{F}}$, and $[\mathbf{q}]$ is the matrix form of the fourth order tensor defined by:

$$\mathbf{q} := \tfrac{1}{3}\mathbf{a}:(\mathbf{I}\otimes\mathbf{I}) - \tfrac{2}{3}(\boldsymbol{\sigma}\otimes\mathbf{I}), \tag{15}$$

also computed at $\mathbf{F} = \bar{\mathbf{F}}$. In expression (14), A_{ipkq} denotes the components of the *first elasticity tensor* [see Marsden and Hughes (1983)].

---

† Note that, in the present formulation, the external load vector coincides with the external load vector of the corresponding standard element. Thus, if configuration dependent loads are considered, the additional *load-stiffness* matrices of the proposed 4-node quadrilateral and 8-node hexahedron are evaluated exactly as for their displacement based counterparts.

‡ In the finite element literature, the tangent stiffness for a standard displacement based element is frequently expressed as the sum of the so called *material* and *geometrical* stiffnesses given, respectively, by

$$\mathbb{K}_e^M = \int_{\varphi(\Omega^e)} \mathbb{B}^T[\mathbf{c}]\mathbb{B}\,dv, \quad \mathbb{K}_e^G = \int_{\varphi(\Omega^e)} \mathbb{G}^T[\mathbf{s}]\mathbb{G}\,dv,$$

where $[\mathbf{c}]$ is the matrix form of the fourth order tensor $c_{jkl} = a_{ijkl}-\sigma_{jl}\delta_{ik}$ and $[\mathbf{s}]$ is the matrix form of the fourth order tensor defined by the components $\sigma_{il}\delta_{jk}$.

Proof. Follows, after lengthy but straightforward manipulations, from the direct application of the formula (12) for the directional derivative of the residual vector.   □

Remark 2.4. The first term on the right hand side of (13) is identical to the tangent stiffness of conventional displacement elements evaluated at $\mathbf{F} = \bar{\mathbf{F}}$. The computation of the extra term indicated in (13) is relatively simple. In addition to the spatial tangent modulus, stress and the discrete gradient at the Gauss point of interest—already used in the calculation of the stiffness of standard elements—only the discrete gradient at the element centroid, $\mathbb{G}_0$, and the matrix [**q**] are required. The evaluation of $\mathbb{G}_0$ is straightforward and, from its definition, the computation of [**q**] also requires little computational effort. Thus, the c.p.u. time needed to compute the tangent stiffnesses of the proposed elements is just slightly longer than that consumed by their kinematically based counterparts. However, it should be noted that the additional stiffness term appearing in (13) is generally *unsymmetric* and, therefore, requires an unsymmetric solver in the finite element computations. We remark that this fact is immaterial whenever the problem to be solved is characterized by an unsymmetric tangent modulus in the continuum setting, i.e., before finite element discretization. This condition is encountered in a wide variety of practical engineering applications, such as, for instance, the simulation of metal forming operations in which frictional contact almost invariably plays an essential role and the use of an unsymmetric solver is inevitable. More sophisticated constitutive laws, such as coupled elasto-plastic damage models (de Souza Neto *et al.*, 1994), employed to predict failure in ductile metals, and non-associative plasticity models in general, also lead to unsymmetric tangent moduli.

Example 2.2.1. The 4-node axisymmetric element. To illustrate the simplicity of the extra stiffness term of expression (13), the explicit form of the matrices involved in its computation is shown here for the axisymmetric version of the 4-node element proposed above. Since the evaluation of the discrete gradient is standard, only the terms required for computation of [**q**] are presented below. Adopting the usual finite element convention, in which the matrix format indices $\{1,2,3,4,5\}$ correspond to the fourth order counterparts $\{11,21,12,22,33\}$, the matrix form of the term $\mathbf{a} : (\mathbf{I} \otimes \mathbf{I})$ that takes part in the definition (15) of **q** is given by

$$[\mathbf{a} :(\mathbf{I} \otimes \mathbf{I})] = \begin{bmatrix} a_{11}+a_{14}+a_{15} & 0 & 0 & a_{11}+a_{14}+a_{15} & a_{11}+a_{14}+a_{15} \\ a_{21}+a_{24}+a_{25} & 0 & 0 & a_{21}+a_{24}+a_{25} & a_{21}+a_{24}+a_{25} \\ a_{31}+a_{34}+a_{35} & 0 & 0 & a_{31}+a_{34}+a_{35} & a_{31}+a_{34}+a_{35} \\ a_{41}+a_{44}+a_{45} & 0 & 0 & a_{41}+a_{44}+a_{45} & a_{41}+a_{44}+a_{45} \\ a_{51}+a_{54}+a_{55} & 0 & 0 & a_{51}+a_{54}+a_{55} & a_{51}+a_{54}+a_{55} \end{bmatrix} \tag{16}$$

where a_{ij} are the components of the matrix counterpart of the spatial tangent modulus **a**. The remaining term $\boldsymbol{\sigma} \otimes \mathbf{I}$ appearing in (15) is simply given by

$$[\boldsymbol{\sigma} \otimes \mathbf{I}] = \begin{bmatrix} \sigma_{11} & 0 & 0 & \sigma_{11} & \sigma_{11} \\ \sigma_{12} & 0 & 0 & \sigma_{12} & \sigma_{12} \\ \sigma_{12} & 0 & 0 & \sigma_{12} & \sigma_{12} \\ \sigma_{22} & 0 & 0 & \sigma_{22} & \sigma_{22} \\ \sigma_{33} & 0 & 0 & \sigma_{33} & \sigma_{33} \end{bmatrix} \tag{17}$$

In the expressions above, the matrix index 5 (or tensorial index 33) represents the circumferential direction, other indices correspond to the in-plane components.

2.3. *Incorporation into existing finite element codes*

As pointed out in remarks 2.2 and 2.4, in addition to the computations carried out normally for the conventional elements, only a few extra operations are required by the

present 4-node quadrilateral and 8-node hexahedron in the evaluation of the internal force vector and the tangent stiffness matrix. This makes the proposed formulation particularly suitable for incorporation into existing finite element codes for large strain analysis of solids. In a code which already supports the standard 4-node quadrilateral (or 8-node brick, if 3-D analysis is sought) and allows access to an unsymmetric solver, the necessary modifications are extremely simple. The routines for calculation of internal force and tangent stiffness can be re-used and easily adapted to accommodate the new elements. The computational procedures for internal force and stiffness evaluation of the proposed elements are schematically illustrated in Boxes 1 and 2, where the corresponding conventional element routines have been extended with the additional operations (framed) required.

2.4. Plane strain implementation

In the *plane strain* case, the modified deformation gradient of expression (5) is redefined as:

$$\bar{\mathbf{F}} := \left[\begin{array}{cc|c} & \bar{\mathbf{F}}_p & 0 \\ & & 0 \\ \hline 0 & 0 & 1 \end{array} \right], \tag{18}$$

where $\bar{\mathbf{F}}_p$ is the assumed modified counterpart of the *plane component*, $\mathbf{F}_p$, of the deformation gradient, defined by:

$$\bar{\mathbf{F}}_p := \left(\frac{\det [\mathbf{F}_{p0}]}{\det [\mathbf{F}_p]} \right)^{1/2} \mathbf{F}_p. \tag{19}$$

Remark 2.5. From (18), the re-defined modified deformation gradient always represents a plane strain state. This would not be the case if the general definition (5) were applied under plane strain conditions. Note that, under the present definition, $(7)_2$ remains valid and pressure distributions within elements will be constant for materials with decoupled volumetric/deviatoric response. Expression $(7)_1$, however, is no longer valid, i.e., the deviatoric component of the modified deformation gradient does not coincide in general with that of the deviatoric deformation gradient that results from the standard bi-linear interpolation at the Gauss points.

Box 1. Element internal force vector computation.

—initialize

> —compute standard $\mathbb{G}$ matrix at $\zeta = 0$
> —evaluate $\det [\mathbf{F}_0]$, with $\mathbf{F}_0 := \mathbf{I} + \mathbb{G}\mathbb{U}$

—set Gauss point coordinates ζ_i and weights w_i

—do $i = 1, 4$ (loop over Gauss points)

   compute standard $\mathbb{G}$ matrix at ζ_i

   $\mathbf{F} := \mathbf{I} + \mathbb{G}\mathbb{U}$

> $\mathbf{F} := \left(\frac{\det [\mathbf{F}_0]}{\det [\mathbf{F}]} \right)^{1/3} \mathbf{F}$ (modified deformation gradient)

   $\sigma := \hat{\sigma}(\mathbf{F})$ (stress computation routine)

   compute standard $\mathbb{B}$ matrix at ζ_i

   $\mathbb{F}_e^{INT} := \mathbb{F}_e^{INT} + w_i \mathbb{B}^{\mathrm{T}} \{\sigma\}$

—end do

—return

The algorithmic implementation of the plane strain version of the proposed 4-node quadrilateral element follows that described in Boxes 1 and 2, except that the exponent 1/3 must be replaced by 1/2 in the computation of the modified deformation gradient. Also, as a consequence of definition (18), expression (15) for the matrix [q], which arises from the linearization of the internal force vector, must be replaced by

$$q := \tfrac{1}{2} a : (I \otimes I) - \tfrac{1}{2}(\sigma \otimes I), \tag{20}$$

in the computation of the element tangent stiffness matrix (Box 2). The explicit form of the matrices [a :(I ⊗ I)] and [σ ⊗ I], in this case, is obtained from expressions (16) and (17) by simply deleting all circumferential components.

Box 2. Element tangent stiffness computation.

—initialize

> —compute standard G matrix at $\zeta = 0$, store in G_0
> —evaluate det $[F_0]$, with $F_0 := I + G_0 U$

—set Gauss point coordinate ζ_i and weights w_i

—do $i = 1, 4$ (loop over Gauss points)

>   compute standard G matrix at ζ_i

> $$F := \left(\frac{\det [F_0]}{\det [F]} \right)^{1/3} F \quad \text{(modified deformation gradient)}$$

> $a := \hat{a}(F)$ (tangent modulus computation routine)
> $K_e := K_e + w_i G^T [a] G$

> > compute matrix q defined by (15)
> > $K_e := K_e + w_i G^T [q] (G_0 - G)$

—end do

—return

---

3. NUMERICAL EXAMPLES

A comprehensive set of numerical examples, involving hyperelastic as well as elastoplastic simulations, is presented in this section. It provides an assessment of the performance of the proposed 4-node quadrilateral and 8-node hexahedron over a wide range of circumstances. Some results obtained here with the present 4-node quadrilateral are compared to similar computations carried out using the geometrically non-linear enhanced strain elements Q1/E4 and Q1/E5, respectively, for plane strain and axisymmetric problems, proposed by Simo and Armero (1992). We remark that the hyperelastic simulations are dealt with within the context of finite elasticity set on the spatial configuration as described by de Souza Neto *et al.* (1995a). In the elastoplastic problems, the framework for treatment of finite multiplicative plasticity based on logarithmic strains described by Perić *et al.* (1992) is adopted.

Example 3.1. Cook's membrane. This example considers the simulation of a tapered and swept panel of unit thickness, illustrated in Fig. 2(a), with one edge clamped and a distributed shearing load $F = 100$ applied to the opposite edge. Plane strain condition is assumed and a regularized neo-Hookean material with shear modulus $\mu = 80.1938$ and bulk modulus $k = 40.0942 \times 10^4$ is adopted. Note that near incompressibility is achieved with the high ratio k/μ, of order 10^4. Several meshes are considered, so that the convergence of the solution with mesh refinement can be assessed. A mesh of 4×4 elements is depicted
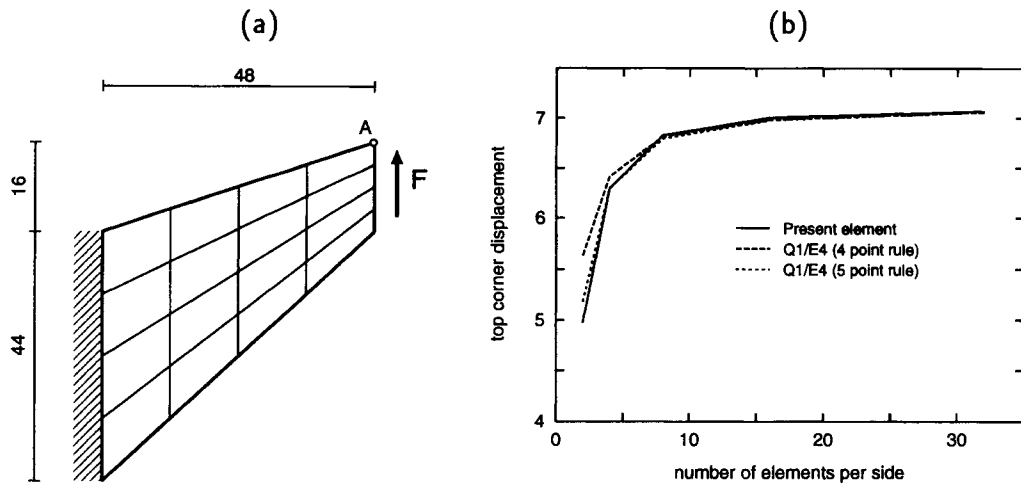
Fig. 2. Cook's membrane. (a) Geometry and boundary conditions; and (b) convergence of the solution with mesh refinement.

in Fig. 2(a). This classical example has been used by Simo and Armero (1992) in the geometrically non-linear range to investigate the convergence properties of the enhanced assumed strain element Q1/E4. Here, the simulations are carried out with the proposed 4-node element and a comparison is made with the solutions obtained with the element Q1/E4 (with 4 and 5 point integration rule). With the present element, for all meshes considered, the total load is applied in 5 increments. The results are shown in the graph of Fig. 2(b) where the final vertical displacement obtained at the upper right corner of the panel (point A of Fig. 2(a)) is plotted against the number of elements per side. It can be seen that the convergence behaviour of the proposed element in this case is almost identical to the behaviour of the element Q1/E4 with 5 point integration rule. With very coarse meshes the Q1/E4 with 4 Gauss points produces slightly better solutions, but in such cases all solutions are very far from the converged result.

Example 3.2. Rubber cylinder pressed between two plates. The simulation of the compression of a rubber cylinder between two frictionless rigid plates is carried out in this example. This problem has been considered by Sussman and Bathe (1987) in the context of the u/p formulation and by Simo and Taylor (1991), who employed a mixed formulation in conjunction with an augmented lagrangian procedure. The geometry of the problem and the boundary conditions are illustrated in Fig. 3(a). Following Sussman and Bathe (1987), two different material models which fit the same experimental data are used: a regularized Mooney-Rivlin material, with constants $C_1 = 0.293$ MPa, $C_2 = 0.177$ MPa and bulk modulus $k = 1410$ MPa, and an Ogden material with coefficients $\mu_1 = 0.746$ MPa, $\mu_2 = -0.306$ MPa, $\mu_3 = 6.609 \times 10^{-5}$ MPa, $\alpha_1 = 1.748$, $\alpha_2 = -1.656$ and $\alpha_3 = 7.671$. Plane strain state is assumed and, for symmetry reasons, only one quarter of the cylinder cross section is considered in the simulation. It is discretized with the mesh of 48 elements shown in Fig. 3(b). The deformed mesh obtained with a prescribed displacement $u = 250$ mm of the plate is depicted in Fig. 3(c). It is in good qualitative agreement with the deformed mesh shown by Simo and Taylor (1991). The reaction forces per unit thickness on the plate, obtained for the Mooney-Rivlin and Ogden models, are plotted in Fig. 4 against the plate deflection u. The curves are plotted up to $u = 200$ mm. For both materials the results agree with Sussman and Bathe (1987).

Example 3.3. Elastomeric bead compression. The numerical simulation of the compression of an elastomeric axisymmetric bead is carried out in this example. The bead—a circular ring with trapezoidal cross section—is schematically represented in Fig. 5. Its function is to provide sealing when the plate, which contacts its top edge, is pressed downwards. In the finite element simulation, the bottom edge of the ring seal is assumed

(a)

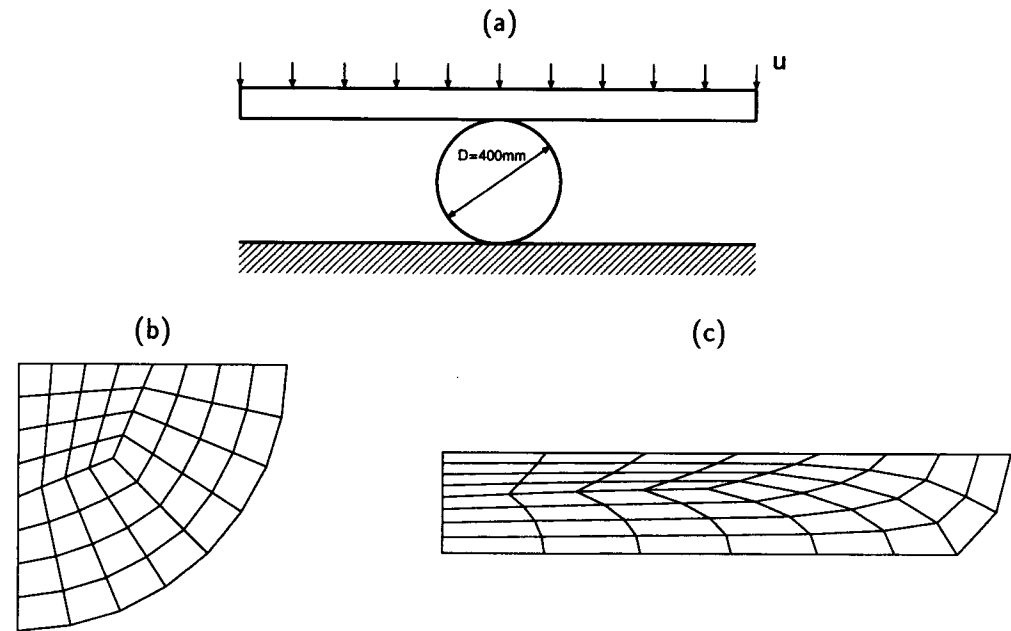**(b)**   **(c)**

Fig. 3. Rubber cylinder pressed between two plates. (a) Geometry and boundary conditions; (b) initial mesh; and (c) deformed mesh at $u = 250$ mm.
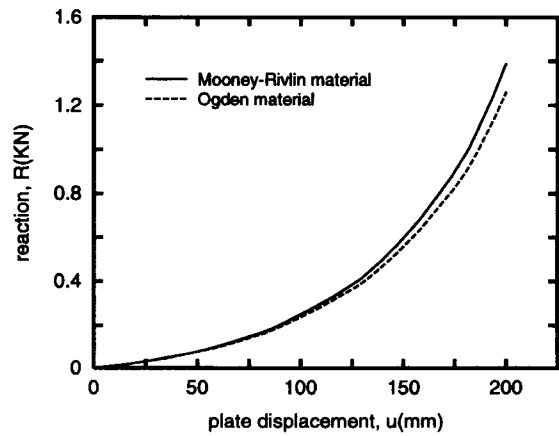

Fig. 4. Rubber cylinder pressed between two plates. Load-deflection curves.

clamped to a flat rigid base and both plate and base are idealized as rigid bodies with frictionless contact condition on the boundaries. The bead is modelled as a regularized neo-Hookean material with constant $C = 2.5$ and bulk modulus $k = 1000$. A mesh of 520
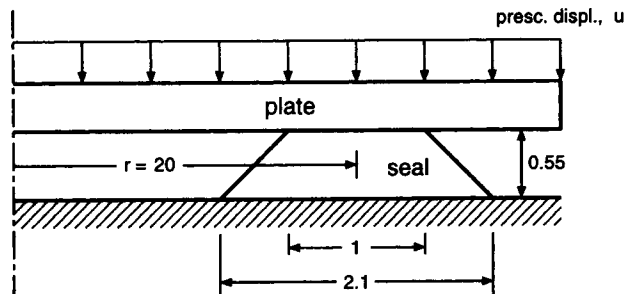
Fig. 5. Elastomeric band compression. Initial geometry and boundary conditions.
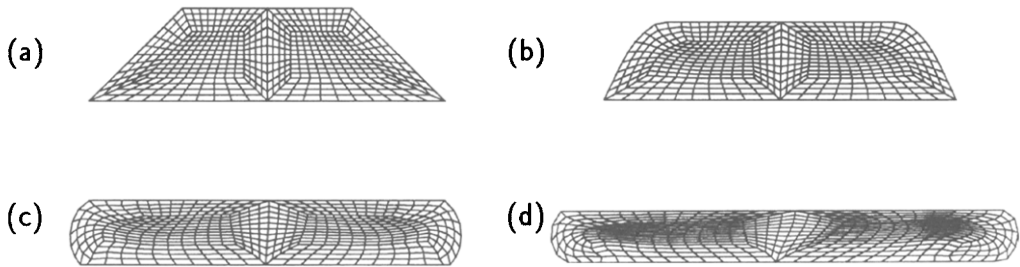
Fig. 6. Elastomeric bead compression. Finite element discretization on the initial configuration and deformed meshes obtained with the present element. (a) Initial configuration; (b) $u = 0.09$; (c) $u = 0.17$; and (d) final configuration, $u = 0.25$.
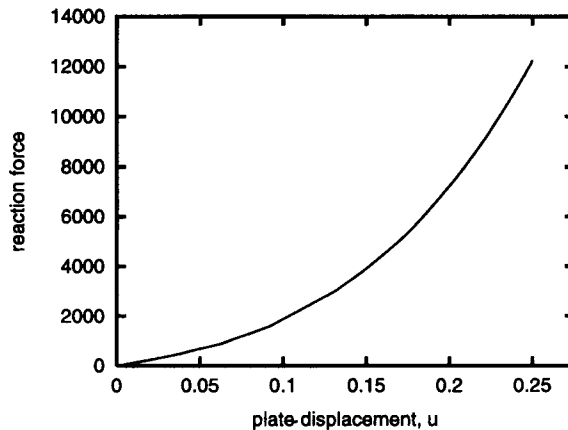

Fig. 7. Elastomeric bead compression. Displacement-reaction diagram.

elements is used to discretize the bead. Figure 6(a) shows the mesh in its initial configuration. The compression of the bead is simulated here with both the axisymmetric version of the 4-node quadrilateral proposed in this paper and the axisymmetric enhanced element Q1/E5. For the enhanced element, the 5 point integration rule is employed in order to avoid spurious mechanisms. With the present element, a total vertical displacement $u = 0.25$ is applied to the plate in 25 increments. Deformed meshes obtained at different stages of the compression process are depicted in Fig. 6(b,c) and (d). They correspond, respectively, to $u = 0.09$, 0.17 and 0.25. At the early stage shown in Fig. 6(b), the lateral surfaces of the seal make contact only with the top plate. At the later stages of Fig. 6(c) and (d), contact also occurs with the rigid base. The reaction-displacement curve obtained is plotted in Fig. 7. The results of the simulation with the Q1/E5 element are shown in Fig. 8. In this case, due to the activation of non-physical hourglass deformation modes, the enhanced element fails to produce meaningful results. Although not severe, spurious hourglass patterns can already be observed in the deformed mesh of Fig. 8(a), obtained with $u = 0.09$. At the later stage depicted in Fig. 8(b), with $u = 2.35$, extremely severe hourglassing has spread throughout the entire structure. The rank deficiency that triggers instability in this class of enhanced elements seems to have been first identified by Wriggers and Reese (1994) in the context of finite hyperelasticity. This fact was later confirmed by Crisfield et al. (1995) and
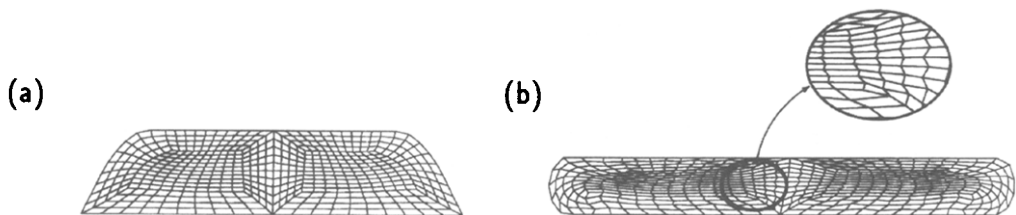

Fig. 8. Elastomeric bead compression. Deformed meshes obtained with the enhanced element Q1/E5 (5 point integration rule). (a) $u = 0.09$; and (b) $u = 0.235$.
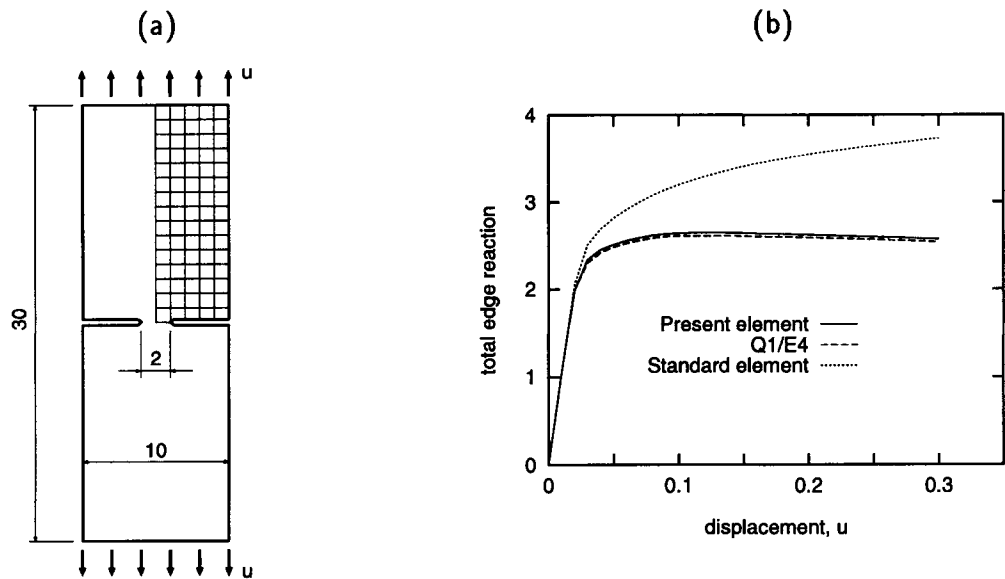
Fig. 9. Stretching of a double notched elastoplastic specimen. (a) Geometry and finite element discretization; and (b) reaction-displacement diagram.

de Souza Neto *et al.* (1995b) for the elasto-plastic case and represents a serious limitation on the applicability of these elements in the finite strain range, particularly under compressive dominant stresses. We remark that, so far, no pathological rank deficiency has been detected in the present formulation.

Example 3.4. Stretching of a double notched specimen. This example considers the plane strain simulation of the stretching of a double notched elastoplastic specimen. The geometry of the problem is illustrated in Fig. 9(a). Only one symmetric quarter of the specimen, discretized by the 5 × 15 element mesh shown in Fig. 9(a), is used in the simulation. The material is assumed to be elastic-perfectly plastic with J_2 flow rule and yield stress:

$$\sigma_y = 0.45$$

The elastic behaviour is defined by the Young's modulus $E = 206.9$ and Poisson ratio $v = 0.29$. This corresponds to the shear and bulk moduli:

$$\mu = 80.1938, \quad k = 164.21.$$

Vertical displacement is applied to the top nodes of the mesh up to a total displacement $u = 0.3$. The simulation is carried out here using the 4-node element presented in this paper as well as the Q1/E4 element and the standard displacement based 4-node quadrilateral. The total edge reactions per unit thickness obtained for each computation is plotted vs the prescribed displacement in Fig. 9(b). It can be seen that both the present element and Q1/E4 are able to predict the existence of a limit load—a phenomenon that is not captured by the standard 4-node quadrilateral. The force-displacement curve predicted by the present formulation is very close to the one obtained with the enhanced element Q1/E4.

Example 3.5. Unconstrained single elastoplastic element test. The purpose of this test is to give an insight into the adequacy of a finite element to capture strain localisation phenomena. It has been used by Simo and Armero (1992) to assess the performance of the enhanced strain element Q1/E4. In this example, the unconstrained element test is carried out for the 4-node element proposed in this paper and the results are compared to similar computations with the Q1/E4 element. For the enhanced element, both 4 and 5 point
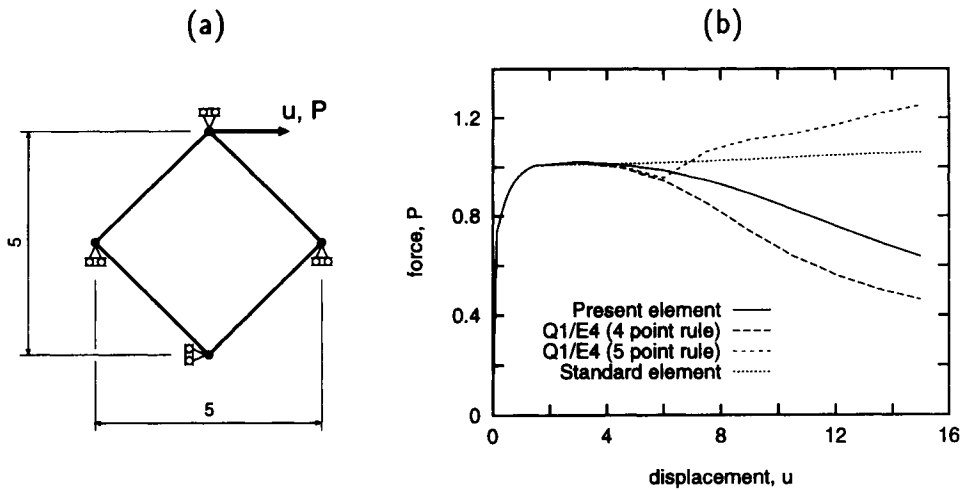
Fig. 10. Single element test. (a) Geometry and load; and (b) force-displacement curve.

integration rules are considered. The problem is schematically represented in Fig. 10(a). The element, with the dimensions and kinematic constraints indicated, is subjected to prescribed horizontal displacement, u, on its top node. Plane strain condition is assumed. The material model used is the same as in the notched specimen example except that the assumption of perfect plasticity is replaced by the following isotropic hardening/softening law:

$$\sigma_y(R) = (\sigma_\infty - \sigma_0)[1 - \exp(-\delta R)] + HR,$$

with constants

$$\sigma_0 = 0.45, \quad \sigma_\infty = 0.715, \quad \delta = 16.93, \quad H = -0.012924.$$

The corresponding force per unit thickness, P, obtained during the tests is plotted in Fig. 10(b). It can be seen that both the proposed element and, as verified by Simo and Armero (1992), the Q1/E4 element with 4 point quadrature are able to capture the global softening that characterizes strain localisation. This indicates a possible suitability of these elements for localisation problems. Interestingly, if the 5 point integration rule suggested by Simo *et al.* (1993) is employed, the forces obtained for the Q1/E4 element increase dramatically after following closely the results for the 4 Gauss point rule up to approximately $u = 6.0$. This phenomenon might be attributed to a bifurcation of the solution and has been noticed by Schönauer *et al.* (1995). The results obtained with the standard 4-node quadrilateral are also plotted and show that, for this element, no softening occurs. The deformed configurations, at $u = 10.0$, of each of the elements discussed are depicted in Fig. 11. The final geometry of the proposed element lies between the deformed geometries of the Q1/E4 with 4 and 5 integration points. We point out the substantial difference which results from the application of distinct quadratures in the Q1/E4 element. Severe locking is exhibited by the standard quadrilateral as a consequence of the pointwise enforcement of the plastic incompressibility constraint.

Example 3.6. Plane strain localisation. This example illustrates the performance of the proposed 4-node quadrilateral under plane strain localisation conditions. It simulates the occurrence of shear bands during the finite stretching of an elastoplastic rectangular bar. This problem has been employed by Simo and Armero (1992) to test the enhanced element Q1/E4. Due to symmetry, only one quarter of the bar is considered in the simulation. Figure 12(a) shows the initial geometry and the finite element mesh used. To trigger strain localisation, a width reduction of 1.8% is introduced in the centre of the bar. The same material constants of the previous example are used. The final deformed mesh obtained
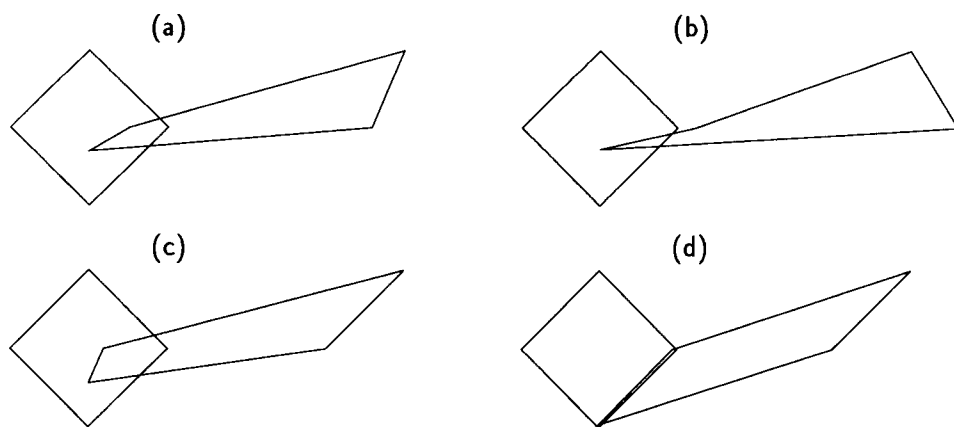
Fig. 11. Single element test. Deformed configurations at $u = 10.0$. (a) Present element; (b) Q1/E4
with 4 point rule; (c) Q1/E4 with 5 point rule; and (d) standard 4-node quadrilateral.

with the present element is shown in Fig. 12(b). It corresponds to a prescribed vertical
displacement $u = 5.0$ on the top nodes of the mesh. The result of the same analysis with
the enhanced element Q1/E4 is plotted in Fig. 12(c) for comparison. For the enhanced
element, the 5 point integration rule has been used in order to avoid the activation of
spurious hourglass modes. The final deformed configurations obtained for both elements
are virtually identical. At that stage, a very localised shear band can be observed. The
performance of the proposed element in this problem can, therefore, be regarded as excel-
lent. It is worth mentioning that, as verified by Simo and Armero (1992), the geometrically
non-linear mean dilatation element Q1/P0 developed by Simo *et al.* (1985) produces a
rather diffuse localisation pattern in the simulation of this problem. The force-displacement
diagrams obtained during the load process are presented in Fig. 13. The results obtained
with the present formulation follow very closely those obtained with the Q1/E4 element.
The substantial decrease in reaction forces occurring near $u = 3.0$ correspond to the devel-
opment of the localised shear band. The curve obtained with the standard 4-node element
is also plotted in Fig. 13 for comparison. In this case, due to excessive constraints on the
displacement field of the conventional 4-node quadrilateral, an over-stiff solution is obtained
and localisation does not occur.

Example 3.7. Necking of an axisymmetric bar. This example consists of the simulation
of the necking of a cylindrical metal bar, with radius 6.413 and length 53.334, in a tensile
test. Simo and Armero (1992) have used this problem to study the performance of the
axisymmetric enhanced element Q1/E5 in large strain localisation problems. The material
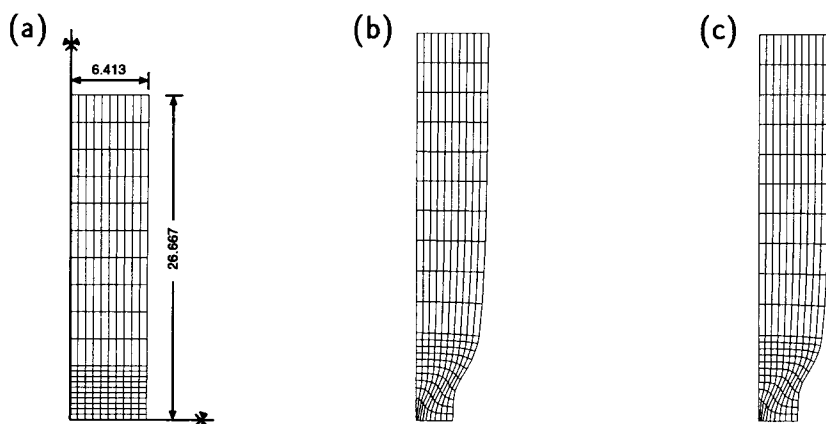

Fig. 12. Plane strain localisation. (a) Initial geometry and finite element mesh; (b) final deformed
mesh ($u = 5.0$) obtained with the present element; and (c) final deformed mesh with element Q1/E4.
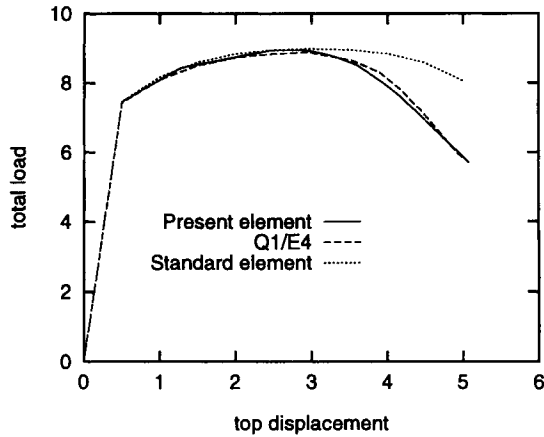
Fig. 13. Plane strain localisation. Force-displacement diagrams.

constants are the same as in the previous two examples, except that the hardening modulus here is taken as:

$$H = 0.12924,$$

so that no material softening occurs. Due to obvious symmetry, only one quarter of the bar is discretized with the appropriate boundary conditions being imposed on the symmetry lines. The mesh of 22×15 4-node axisymmetric elements shown in Fig. 14(a) is used. A geometric imperfection of 1.8% of the radius is introduced at the centre of the bar to trigger the necking. A vertical displacement $u = 7.0$ is imposed incrementally at the top of the bar. The final deformed mesh, in which the development of necking in the central zone can be clearly seen, is plotted in Fig. 14(b). Its shape is in agreement with the result obtained by Simo and Armero (1992) with the enhanced element Q1/E5. We remark that the occurrence of severe spurious hourglassing in the localised region has been observed by Simo and Armero (1992) in the simulation of this problem with the axisymmetric version of the mean dilatation element Q1/P0. Constant pressure within one element, as in the Q1/P0 element, is obtained with the present formulation for the material considered in this example. Nevertheless, in contrast to the Q1/P0 formulation, spurious hourglass patterns are not
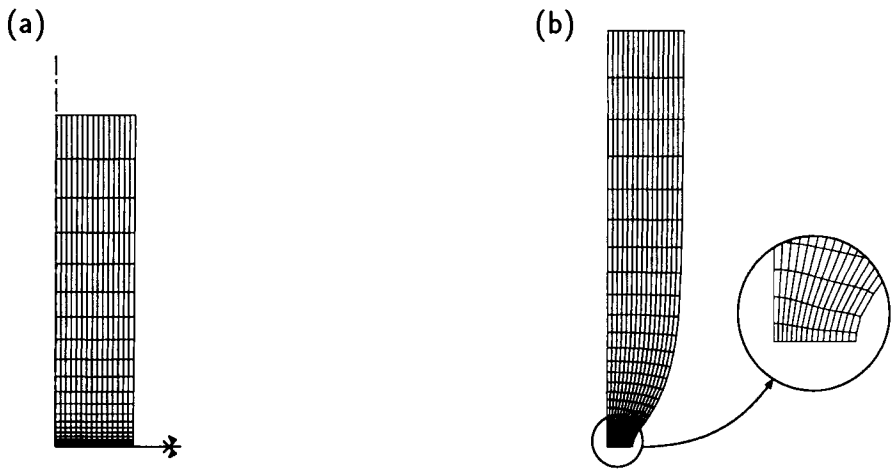

Fig. 14. Axisymmetric necking. (a) Initial mesh; and (b) deformed mesh with imposed displacement $u = 7.0$.
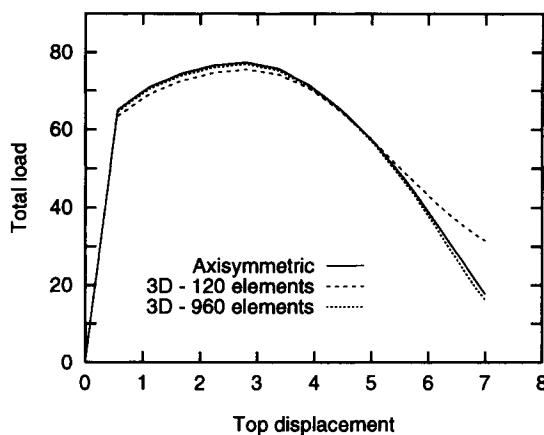
Fig. 15. Axisymmetric and 3-D necking. Force-displacement diagrams.

detected here. Figure 15 shows the reaction-displacement diagram obtained in the present computation. The reactions obtained for an equivalent 3-D simulation, to be discussed in Example 3.9 below, are also plotted. The present result is in close agreement with the curve obtained by Simo and Armero with the Q1/E5 element.

Example 3.8. Adaptive analysis of the upsetting of an elastoplatic billet. Due to the large element distortions involved, as well as accuracy considerations, many practical finite strain problems can be solved only if the finite element mesh is redefined at some stage of the solution procedure. Whenever a new mesh is chosen, all relevant variables that define the problem at hand must be appropriately transferred from the old mesh to the new mesh so that the solution process can continue. Formulations such as enhanced assumed strain methods (Simo and Armero, 1992) and incompatible modes elements (Crisfield *et al.*, 1995) are based on the enrichment of the element strain field with internal deformation modes defined by a set of local internal parameters. For such methodologies, the appropriate transfer of local parameters between meshes is crucial and, at present, it seems not to be clear. In contrast, such an issue does not arise for the elements proposed in this paper. The absence of element internal parameters makes the incorporation of the present elements within an adaptive remeshing environment rather straightforward. Indeed, exactly as for standard displacement based formulations, the present elements require only nodal displacements and *physical* internal variables (plastic strain, hardening parameters, etc.) to be transferred between meshes. The objective of this example is to illustrate the suitability of the present elements for adaptive mesh refinement.

The problem here consists of the simulation of the upsetting of a cylindrical elastoplastic billet. The billet, with radius $r = 9$ mm and height $h = 30$ mm is compressed between two flat tools (assumed rigid) subjected to sticking contact condition on the interface. As in the previous elastoplastic examples, a J_2 elastoplastic material is assumed, but here a *linear* hardening rule is adopted:

$$\sigma_y(R) = HR,$$

with hardening modulus $H = 0.7$ MPa. The Young's modulus and Poisson ratio are, respectively, $E = 200.0$ and $v = 0.3$, corresponding to:

$$\mu = 76.92\,\text{MPa}, \quad k = 166.67.$$

The initial tool/workpiece configuration is schematically illustrated in Fig. 16(a). The initial mesh employed to discretize the symmetric quarter of the cylinder is plotted in Fig. 16(b). The criterion for mesh refinement/de-refinement is based on the incremental plastic work [see Perić *et al.* (1994)]. Two other meshes, generated during the adaptive analysis, are shown in Figs 16(c) and 16(d). The configurations illustrated correspond to 40% and 70%
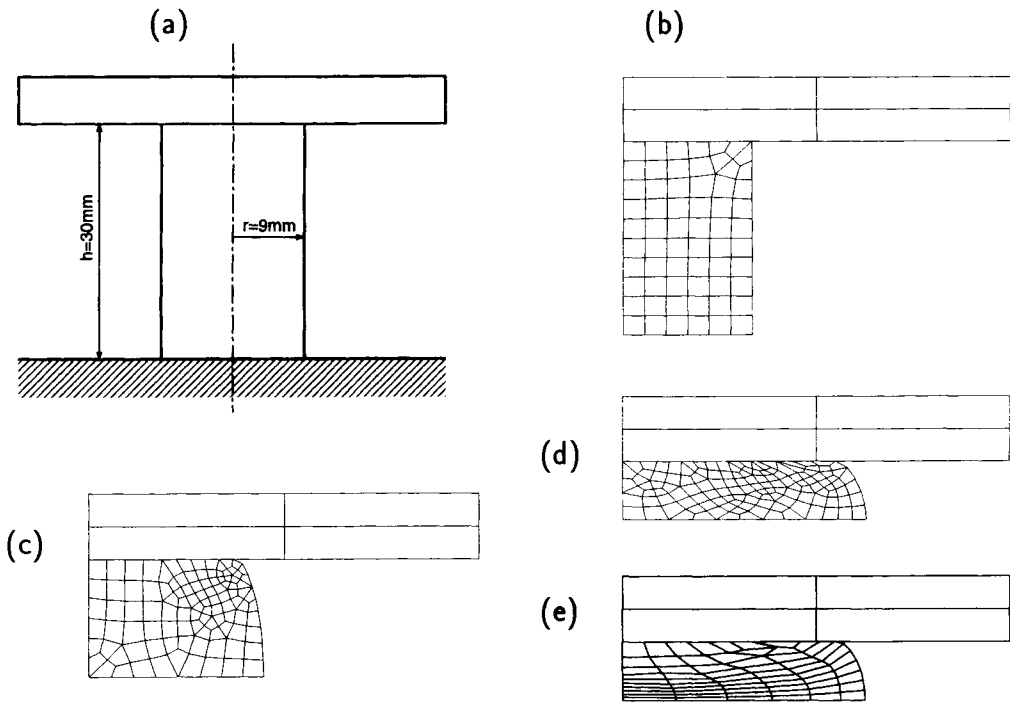
Fig. 16. Adaptive analysis. (a) Initial tool/work piece configuration; (b) initial mesh; (c) deformed mesh at 40% compression; (d) deformed mesh at 70% compression; and (e) deformed mesh at 70% compression *without remeshing*.

compression of the billet respectively. Due to the concentration of the plastic process near the corner of the billet, substantial refinement is detected in that region of the mesh of Fig. 16(c). At the later stage of 70% compression (Fig. 16(d)) the rate of plastic dissipation, and, therefore, the elements, are more equally distributed. Note that, at any instant, all elements have a very good aspect ratio. The result of a similar computation without adaptivity, i.e., maintaining the initial discretization throughout the entire process, is shown in Fig. 16(e).

Example 3.9. Three-dimensional necking of a cylindrical bar. A three-dimensional analysis of the problem of the necking of the cylindrical bar described in Example 3.7 is carried out here. The objective is to assess the performance of the 8-node brick element proposed in this paper. The geometry and material properties are the same as in Example 3.7. Two different meshes, of 120 and 960 three-dimensional elements, shown in Fig. 17 are used to discretize the symmetric octant of the specimen, with the appropriate boundary
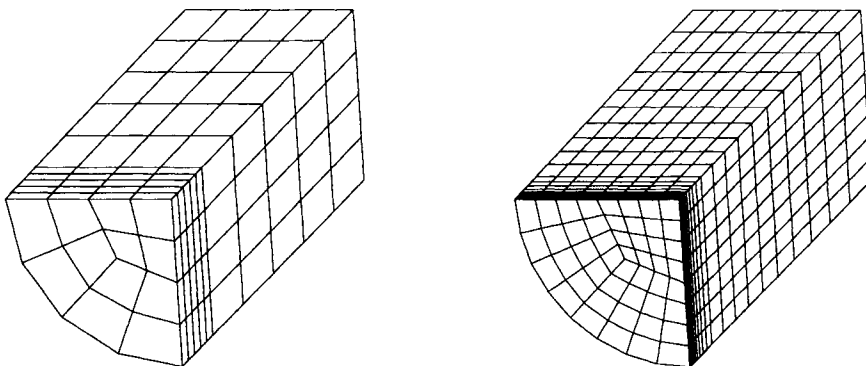

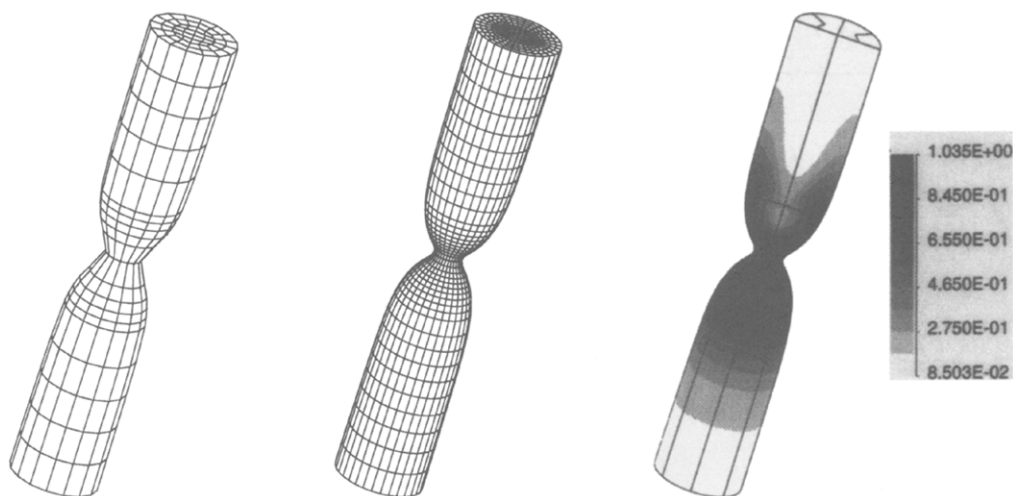Fig. 17. Three-dimensional necking of a cylindrical bar. Initial meshes.

Fig. 18. Three-dimensional necking of a cylindrical bar. Deformed configurations at $u = 7.0$ and effective stress contour plot.

conditions imposed on the symmetry planes. The final deformed configurations (corresponding to $u = 7.0$) obtained for both meshes are shown in Fig. 18 along with the effective stress contour plot obtained for the finer mesh. It can be seen that the two meshes are able to predict correctly the necking phenomenon. This illustrates the suitability of the proposed 8-node hexahedron for problems involving strain localisation. We remark that the final shape resulting from the simulation with 960 eight-node hexahedra is virtually identical to that predicted by the simulation reported in Example 3.7, in which 330 axisymmetric 4-node quadrilaterals have been employed. The force-displacement curves obtained for both 3-D simulations are plotted in Fig. 15 along with results of the axisymmetric analysis. The results for the finer 3-D mesh are almost undistinguishable from those obtained in the axisymmetric simulation. We remark that in a similar simulation with the 3-D version of the Q1/P0 element, the occurrence of extremely severe spurious hourglassing has been observed by Simo and Armero (1992). Figure 19(a) is reproduced from Simo and Armero (1992) and shows the non-physical hourglass patterns spread throughout the localised zone. Again, as in Example 3.7 and in contrast to the mean dilation formulation, spurious hourglassing is not observed with the present element. This is clearly illustrated in Fig. 19(b).

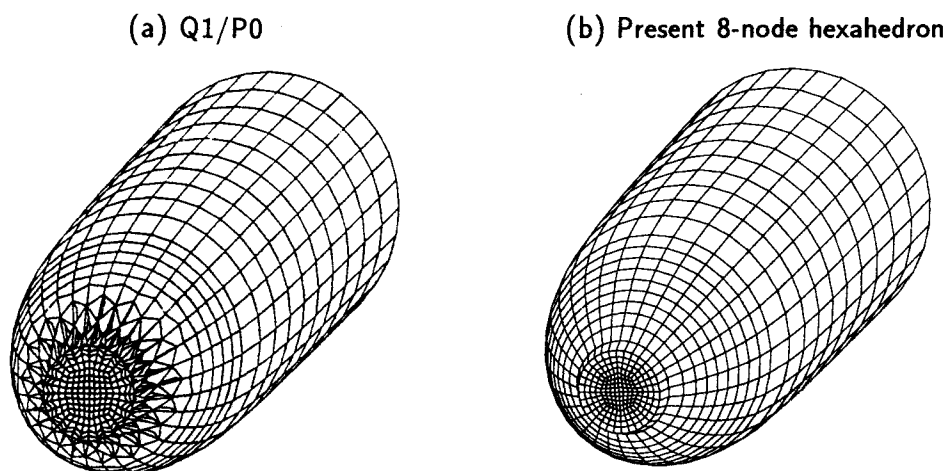## (a) Q1/P0   (b) Present 8-node hexahedron

Fig. 19. Three-dimensional necking of a cylindrical bar. Transversal cross sections at $u = 7.0$. (a) Results for the mean dilation Q1/P0 element (reproduced from Simo and Armero, 1992) and (b) present 8-node element.

4. CONCLUSION

A four-node quadrilateral and an eight-node hexahedron for finite strain analysis of nearly incompressible solids have been proposed. Based on the deviatoric/volumetric decomposition in conjunction with the replacement of the deformation gradient with an assumed modified counterpart, the proposed elements are simple and can be applied with arbitrary material models. Despite the conceptual similarities, the present approach cannot be classed as a geometrically non-linear *B-bar* method.

The closed form of the corresponding consistent tangent stiffness matrices has been derived. It possesses a very simple structure but is unsymmetric even for materials with a symmetric tangent modulus. Such a loss of symmetry, however, does not imply extra computational effort whenever the continuum problem is characterized by an unsymmetric tangent modulus.

It has been shown that the implementation of the proposed elements in current codes is straightforward. The new elements are obtained with the introduction of very simple changes in the routines for computation of internal force and tangent stiffness of the standard displacement based 4-node quadrilateral and 8-node brick. The strain driven nature of the algorithms for integration of inelastic constitutive laws employed in standard displacement based formulations is preserved.

By means of numerical examples, the performance of the elements has been tested over a wide range of applications. A very good behaviour, without the occurence of spurious locking or hourglassing modes, has been observed in problems involving nearly incompressible hyperelasticity and finite multiplicative plasticity. Interestingly, a remarkable ability in capturing strain localisation phenomena has been verified for both plane strain and axisymmetric versions of the proposed 4-node quadrilateral as well as for the 8-node hexahedron. Due to the absence of internal parameters, in contrast to assumed enhanced strain and incompatible modes elements, the present formulation has proven particularly suitable for adaptive mesh refinement.

Finally, we remark that the approach adopted in this paper can be easily extended into a general methodology for the formulation of improved low order plane, axisymmetric and three-dimensional elements for geometrically non-linear quasi-incompressible analysis. This will be the subject of a follow-up publication.

REFERENCES

Crisfield, M. A., Moita, G. F., Jelenić, G. and Lyons, L. P. R. (1995). Enhanced lower-order element formulations for large strains. *Proceedings of the Fourth International Conference on Computational Plasticity: Fundamentals and Applications—Barcelona* (Eds D. R. J. Owen *et al.*). Pineridge Press, UK.

Hughes, T. J. R. (1980). Generalization of selective integration procedures to anisotropic and nonlinear media. *Int. J. Num. Meth. Engng* **15**, 1413–1418.

Marsden, J. E. and Hughes, T. J. R. (1983). *Mathematical Foundations of Elasticity*. Prentice-Hall, Englewood Cliffs, NJ.

Moran, B., Ortiz, M. and Shih, F. (1990). Formulation of implicit finite element methods for multiplicative finite deformation plasticity. *Int. J. Num. Meth. Engng* **29**, 483–514.

Ortiz, M. and Popov, E. P. (1985). Accuracy and stability of integration algorithms for elastoplastic constitutive relations. *Int. J. Num. Meth. Engng* **21**, 1561–1576.

Perić, D., Owen, D. R. J. and Honnor, M. E. (1992). A model for finite strain elasto-plasticity based on logarithmic strains: computational issues. *Comp. Meth. Appl. Mech Engng* **94**, 35–61.

Perić, D., Yu, J. and Owen, D. R. J. (1994). On error estimates and adaptivity in elastoplastic solids: application to the numerical simulation of strain localization in classical and Gosserat continua. *Int. J. Num. Meth. Engng* **37**, 1351–1379.

Schönauer, M., de Souza Neto, E. A. and Owen, D. R. J. (1995). Hencky tensor based enhanced large strain element for elasto-plastic analysis. *Proceedings of the Fourth International Conference on Computational Plasticity: Fundamentals and Applications—Barcelona* (Eds D. R. J. Owen *et al.*). Pineridge Press, UK.

Simo, J. C. and Armero, F. (1992). Geometrically non-linear enhanced strain mixed methods and the method of incompatible modes. *Int. J. Num. Meth. Engng* **33**, 1413–1449.

Simo, J. C., and Hughes, T. R. J. (1987). General return mapping algorithms for rate-independent plasticity. *Constitutive Laws for Engineering Materials: Theory and Applications* (Eds C. S. Desai *et al.*). Elsevier, Oxford.

Simo, J. C. and Rifai, S. (1990) A class of mixed assumed strain methods and the method of incompatible modes. *Int. J. Num. Meth. Engng* **29**, 1595–1638.

Simo, J. C. and Taylor, R. L. (1991). Quasi-incompressible finite elasticity in principal stretches. Continuum basis and numerical algorithms. *Comp. Meth. Appl. Mech. Engng* **85**, 273–310.

Simo, J. C., Taylor, R. L. and Pister, K. S. (1985). Variational and projection methods for the volume constraint in finite deformation elasto-plasticity. *Comp. Meth. Appl. Mech. Engng* **51**, 177–208.

Simo, J. C., Armero, F. and Taylor, R. L. (1993). Improved versions of assumed enhanced strain tri-linear elements for 3D finite deformation problems. *Comp. Meth. Appl. Mech. Engng* **110**, 359–386.

de Souza Neto, E. A., Perić, D. and Owen, D. R. J. (1994). A model for elasto-plastic damage at finite strains : computational issues and applications. *Engng Comp.* **11**, 257–281.

de Souza Neto, E. A., Perić, D. and Owen, D. R. J. (1995a). Finite elasticity in spatial description : linearization aspects with 3-D membrane applications. *Int. J. Num. Meth. Engng* **38**, 3365–3381.

de Souza Neto, E. A., Perić, D., Huang, G. C. and Owen, D. R. J. (1995b). Remarks on the stability of enhanced strain elements in finite elasticity and elastoplasticity. *Proceedings of the Fourth International Conference on Computational Plasticity : Fundamentals and Applications—Barcelona* (Eds D. R. J. Owen *et al.*). Pineridge Press, UK. [Also in *Commun. Num. Meth. Engng* **11**, 951–961.]

Sussman, T. and Bathe, K.-J. (1987). A finite element formulation for nonlinear incompressible elastic and inelastic analysis. *Comp. Struct.* **26**, 357–409.

Taylor, R. L., Beresford, P. J. and Wilson, E. L. (1976). A non-conforming element for stress analysis. *Int. J. Num. Meth. Engng* **10**, 1211–1219.

Wriggers, P. and Reese, S. (1994). A note on enhanced strain methods for large deformations. *Comp. Meth. Appl. Mech. Engng* (Submitted for publication).